Physics of Plasmas ARTICLE scitation.org/journal/php

Gyrokinetic particle simulations of interactions between energetic particles and magnetic islands induced by neoclassical tearing modes

Cite as: Phys. Plasmas **27**, 032508 (2020); doi: 10.1063/1.5126681
Submitted: 4 September 2019 · Accepted: 18 February 2020 ·
Published Online: 24 March 2020

View Online Export Citation CrossMark

X. Tang,[1,2] Z. Lin,[2,a)] W. W. Heidbrink,[2] J. Bao,[3] C. Xiao,[1] Z. Li,[4] J. Li,[5] and L. Bardóczi[4]

AFFILIATIONS

[1]Fusion Simulation Center, Peking University, Beijing 100871, China
[2]Department of Physics and Astronomy, University of California, Irvine, California 92697, USA
[3]Beijing National Laboratory for Condensed Matter Physics and CAS Key Laboratory of Soft Matter Physics, Institute of Physics, Chinese Academy of Sciences, Beijing 100871, China
[4]General Atomics, San Diego, California 92186, USA
[5]Department of Physics, Nankai University, Tianjin 300071, China

[a)]Author to whom correspondence should be addressed: zhihongl@uci.edu

ABSTRACT

Interactions between energetic particles (EPs) and neoclassical tearing mode (NTM) islands in the DIII-D tokamak are studied using the global gyrokinetic toroidal code (GTC). GTC simulations find that the EP radial profile is partially flattened within the magnetic island regions and that there are stochastic regions in the particle phase space. Radial particle flux is induced mainly around the magnetic island regions and decreases with time to almost zero when the initial EP distribution achieves a new steady-state in the absence of EP sources. Stochastic regions of magnetic field lines induced by the superposition of multiple islands have weak effects on the particle flux when the width of stochastic regions is smaller than the EP drift orbit width. The perturbed parallel EP current induced by the magnetic islands has weak stabilizing effects on the linear growth rate of the NTM instability in this DIII-D experiment.

Published under license by AIP Publishing. https://doi.org/10.1063/1.5126681

I. INTRODUCTION

In tokamak fusion experiments, neoclassical tearing mode (NTM) is one of the most dangerous magnetohydrodynamic (MHD) instabilities, which is mainly driven by bootstrap current induced by plasma pressure gradients. The NTM can produce large magnetic islands on $q = m/n$ rational surfaces, where q is the safety factor and m and n are the poloidal and toroidal mode numbers. The NTM islands can destroy the topology of magnetic flux surfaces, degrade plasma confinement, and lead to disruption.[1] For example, magnetic islands can induce large energetic particle (EP) transport in tokamaks.[2–8] The EP loss not only degrades the fusion confinement but can also be detrimental to the divertor and limiter due to the high energy flux of EPs, which can cause material sputtering.[9] Furthermore, a reduction in neutral beam-driven current by the magnetic islands has been observed in the DIII-D tokamak.[10] The effects of magnetic islands on the EP confinement in tokamaks have previously been studied theoretically. For example, it has been shown[11] that the orbits of circulating EPs can become stochastic when the island width and the EP curvature drift exceed some thresholds. A fast method[12] to determine the broken Kolmogorov–Arnold–Moser (KAM) surface domain in the phase space has been used to predict the EP distribution in the presence of a spectrum of MHD modes.

Meanwhile, many fusion experiments have shown that EPs can have effects on the stability of tearing mode (TM) and NTM.[3,13,14] In the EAST tokamak,[14] it has been observed that the magnetic island width and rotation frequency oscillate due to the interaction between EPs and the magnetic islands. In the DIII-D tokamak,[3] a modulation of various neutral beam sources has been used to study the interactions of EPs with the TM, which changes the island width by a few millimeters. Theoretical work has also predicted that the growth rate of the NTM can be affected by the EP.[15–19] Reference 16 shows that the counter-circulating EPs have destabilizing effects and co-circulating EPs have weakly stabilizing effects on the NTM. Reference 19 shows that when the EP density peaks outside the low-order rational surfaces,

Published under license by AIP Publishing

the growth of the magnetic island can be suppressed by the EP helical current induced by the islands. Therefore, understanding the EP re-distribution by the magnetic islands and the EP effects on the NTM excitation is important for improving EP confinement in tokamak plasmas. A predictive capability of the EP distribution function with islands is also essential for the future fusion experiments in ITER.[20]

In this paper, the global gyrokinetic toroidal code (GTC) is used to calculate the EP transport caused by static islands and the effects of perturbed EP current on the linear growth rate of the NTM in the DIII-D experiments. Our simulations find that the EP radial profile is partially flattened within the magnetic island regions. Radial EP flux is induced around the magnetic island regions due to stochasticity in the EP phase space. For multiple magnetic islands, stochastic regions of magnetic field lines in real space are smaller than the EP orbit width and thus have weak effects on the EP flux. Finally, we use the resistive MHD simulation model[21] in the GTC to study the EP effects on the linear growth rate of the NTM. The perturbed EP current induced by the NTM islands has a weakly stabilizing effect on the linear growth rate of the NTM for the DIII-D experiment used in the GTC simulations.

This paper is organized as follows: Plasma equilibrium profiles and simulation models are described in Sec. II. Section III describes the implementation of static magnetic islands. The EP re-distribution by the static islands is studied in Sec. IV. Section V presents resistive MHD simulations of the EP effects on the NTM linear growth rates. Summary is drawn in Sec. VI.

II. SIMULATION MODEL AND EXPERIMENTAL EQUILIBRIUM

The GTC[22] uses the particle-in-cell method to study kinetic effects in low frequency (below ion cyclotron frequency) instabilities in toroidal plasmas. The GTC has been extensively used to study microturbulence, EP instabilities, MHD modes, and the effects of magnetic islands on microturbulence[23,24] and bootstrap current in toroidal plasmas.[25] The gyrokinetic simulation model[26] of the GTC is utilized to study the re-distribution of EPs by NTM and the effects of EPs on the NTM excitation. The GTC uses Boozer coordinates (ψ, θ, ζ), where ψ is the poloidal flux, θ is the poloidal angle, and ζ is the toroidal angle. The magnetic field[27] in the GTC can be expressed in the covariant form as $\boldsymbol{B}_0 = I\nabla\theta + g\nabla\zeta$, where g and I are the poloidal and toroidal currents (divided by 2π), respectively. The contravariant representation is given by $\boldsymbol{B}_0 = q\nabla\psi \times \nabla\theta - \nabla\psi \times \nabla\zeta$, where q is the safety factor. The collisionless gyrokinetic equation governing the evolution of the EP distribution function in the guiding center coordinates $(\boldsymbol{R}, \mu, v_{||})$ is[28,29]

$$\frac{d}{dt}f(\boldsymbol{R}, \mu, v_{||}, t) \equiv \left(\frac{\partial}{\partial t} + \dot{\boldsymbol{R}}\cdot\nabla + \dot{v}_{||}\frac{\partial}{\partial v_{||}}\right)f = 0, \tag{1}$$

where $\mathbf{R}$ represents the spatial coordinates of the gyrocenter μ and $v_{||}$ are the magnetic momentum and parallel velocity, respectively. The equation of motion for the gyrocenter is

$$\frac{d\boldsymbol{R}}{dt} = v_{||}\frac{\boldsymbol{B}}{B_0} + \boldsymbol{v}_E + \boldsymbol{v}_d, \tag{2}$$

where $\boldsymbol{v}_d$ is the magnetic drift velocity $\boldsymbol{v}_d = \frac{v_{||}^2}{\Omega_\alpha}\nabla\times\boldsymbol{b}_0 + \frac{\mu}{m_\alpha\Omega_\alpha}\boldsymbol{b}_0 \times \nabla B_0$, and $\boldsymbol{v}_E$ is the E × B drift velocity $\boldsymbol{v}_E = \frac{c\boldsymbol{b}_0\times\nabla\phi}{B_0}$. $\boldsymbol{B}_0 = B_0\boldsymbol{b}_0$ is the equilibrium magnetic field, $\boldsymbol{B} = \boldsymbol{B}_0 + \delta\boldsymbol{B}$, and c and t denote the light speed and time, respectively. The parallel acceleration due to the mirror force and parallel electric fields is written as

$$\frac{dv_{||}}{dt} = -\frac{1}{m_\alpha}\frac{\boldsymbol{B}^*}{B_0}\cdot(\mu\nabla\boldsymbol{B}_0 + Z_\alpha\nabla\phi) - \frac{Z_\alpha}{m_\alpha c}\frac{\partial A_{||}}{\partial t}. \tag{3}$$

Here, index $\alpha = e, i$ stands for the particle species (electron or ion), m_α is the particle mass, Z_α is the particle charge, and Ω_α is the cyclotron frequency. $\boldsymbol{B}^* = \boldsymbol{B}_0 + \frac{B_0 v_{||}}{\Omega_\alpha}\nabla\times b_0 + \delta\boldsymbol{B}$, where $\delta\boldsymbol{B}$ denotes the perturbed magnetic field $\delta\boldsymbol{B} = \nabla\times\delta A_{||}\boldsymbol{b}_0$ and $A_{||}$ is the parallel vector potential. The electrostatic ϕ and vector potential $A_{||}$ are gyro-averaged for EPs.

To study the EP re-distribution by the magnetic islands, the GTC is used to follow EP trajectories in a realistic equilibrium of DIII-D shot #157402, where stationary magnetic islands have been measured by electron cyclotron emission (ECE). Experimentally, this shot was designed to study the effects of NTM on the re-distribution of EPs with a major radius of the magnetic axis $R_0 = 1.78$ m and an on-axis equilibrium magnetic field of $B_a = 1.95$ T. In our simulation, the EP birth population is obtained from TRANSP[30] calculations as shown in Figs. 1(a) and 1(b). The distributions are obtained after integrating over all magnetic surfaces. Note that, in TRANSP modeling, the EP population is described in (R, Z, λ, E) coordinates, where R is the major radius, Z is the vertical coordinate, λ is the pitch angle $\lambda = v_{||}/v$, and E is the kinetic energy. Therefore, we need to map from the Cartesian coordinates (R, Z) into Boozer coordinates (ψ, θ). Because of the axis-symmetry, we set the value of the toroidal angle ζ as a random number between 0 and 2π for each EP particle. The coordinates (λ, E) are then converted to $(v_{||}, \mu)$ used in the GTC.

In Fig. 1, the energy distribution of EP birth population roughly satisfies the slowing-down distribution with a peak of energy at $E = 25$ keV and a peak of pitch angle at $\lambda = 0.6$. There are both co- and counter-EPs in the birth population as shown in Fig. 1(a).

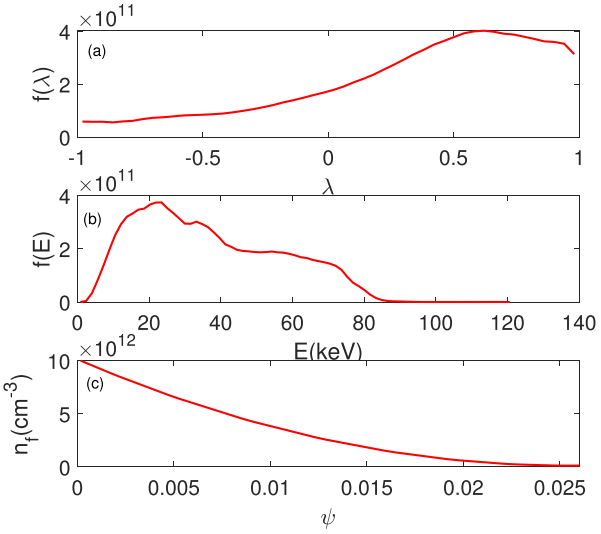

FIG. 1. EP distribution function in the pitch angle $\lambda = v_{||}/v$ space (a) and energy E space (b) and radial profile of the EP density (c).

Published under license by AIP Publishing

The radial density profile of EPs is shown in Fig. 1(c). The density peaks on the magnetic axis and decreases toward the boundary. The percentage of trapped particles is about 28%. We consider $\mu B_m > E$ as the condition for trapped particles, where B_m is the maximal magnetic field on the flux-surface.

III. IMPLEMENTATION OF STATIC ISLANDS FROM EXPERIMENTAL DATA

In our simulation, the static island width is calculated from the experimental data of the electron temperature T_e for the DIII-D shot #157402. The 2-dimensional structure (location and width) of the magnetic islands is estimated by a helical reconstruction of T_e, which is probed using a DIII-D electron cyclotron (ECE) radiometer.[31] This system provides T_e from measurements using optically thick, second harmonic (X-mode) electron cyclotron emission in 40 radial locations with a sampling rate of 480 kHz in the tokamak mid-plane. The ECE channel locations are shown by black circles in Fig. 2(a). T_e is transformed from the laboratory frame to the island frame by mapping from time t to helical angle $\xi = m\theta - n\zeta$ via phase-locking analysis as described in Ref. 32 [see Fig. 2(a)]. These islands are close to the q = 2 rational surface ($R = 201$ cm), and the poloidal and toroidal structures of magnetic fluctuations are consistent with m/n = 2/1 mode numbers. Figure 2(b) shows T_e profiles through the X-point at ($\xi = 0$) and O-point at ($\xi = \pi$). Note that the T_e O-point profile is nearly flat as expected. A small T_e peaking is observed, which can be caused by heat sources within the island.

Figure 3(a) shows the radial profiles of the electron temperature without NTM (T_{e0}) and the temperature with the magnetic island O-point (T_e). From the experimental data T_e and T_{e0}, we can obtain the perturbed poloidal flux $\delta\psi$ by the following expression:

$$\delta T_e = \frac{\partial T_{e0}}{\partial \psi} \cdot \delta\psi, \tag{4}$$

where $\delta T_e = T_e - T_{e0}$, and both T_{e0} and T_e only depend on the poloidal flux function. The profile of the perturbed poloidal flux $\delta\psi$ obtained from Eq. (4) is plotted in Fig. 3(b). The tearing mode activity is also detected by toroidal and poloidal arrays of magnetic probes. The magnetic frequency spectrum only shows power at 10.75 kHz and higher harmonics such as 21.5 kHz and 32 kHz. The analysis of the toroidal data indicates that the 10.75 kHz mode has toroidal mode number $n = 1$; the ratio of amplitudes at the probe for the 21.5 kHz mode relative to the 10.75 kHz mode is 0.12 ± 0.02. The analysis of the poloidal array indicates that the 10.75 kHz mode is predominately $m = 2$, but there is also a large $m = 4$ component of comparable magnitude. In

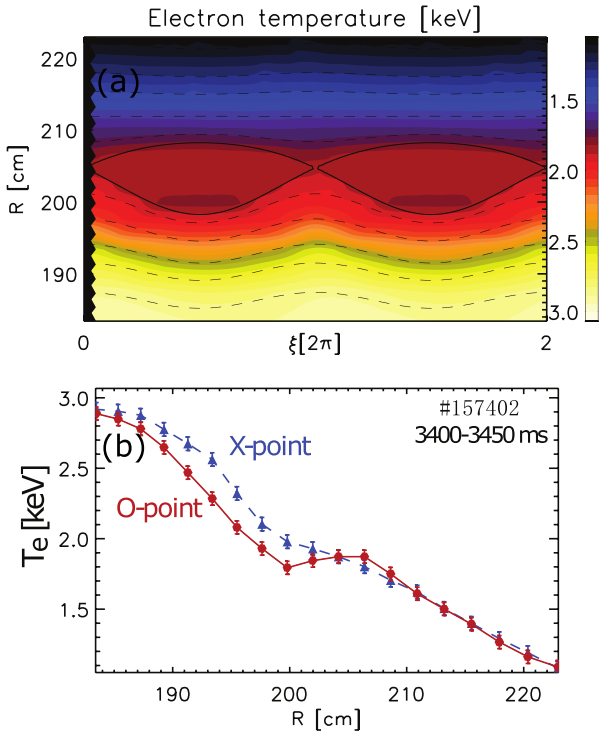

FIG. 2. (a) Contour of electron temperature measured by a horizontal ECE radiometer vs major radius R. The horizontal axis is the helical angle ξ. Here, the phase locked $T_e(\xi, R)$ data are plotted twice for visualization purposes, and the expected separatrices are over-plotted with black solid lines. (b) Temperature profiles when the X-point and O-point are aligned with the radiometer toroidal angle in the mid-plane.

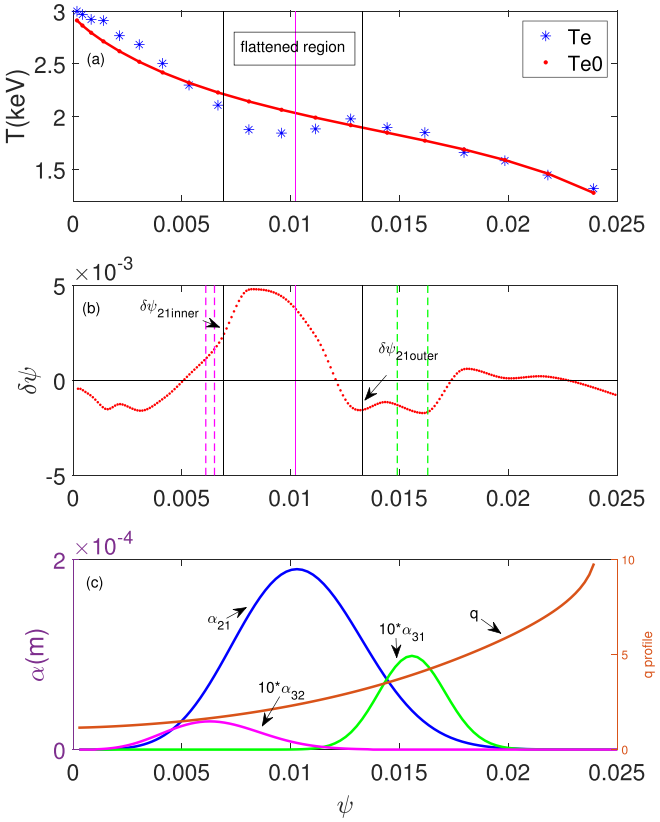

FIG. 3. (a) Time average electron temperature profiles without NTM (T_{e0}) and with NTM (T_e) measured by ECE. The purple line is the q = 2 surface, and the black lines are separatrices of the 2/1 island. (b) Profile of perturbed poloidal flux function $\delta\psi$. Both ψ and $\delta\psi$ are normalized by $B_a R_0^2$. Separatrices for the three islands are marked by vertical lines with different colors. (c) Profiles of safety factor q and three island amplitudes $\alpha_{m/n}$(m).

Published under license by AIP Publishing

addition, fitting to the poloidal data finds that the ratio of the $m = 3$ to $m = 2$ amplitude is 0.33 ± 0.13.

Although the magnetic data suggest that there could be mode-locked islands at the q = 3/2 and q = 3/1 surfaces, the ECE data indicate that, if these islands exist at all, they are quite small. As shown in Fig. 3, the ECE data show clear evidence of island formation at the q = 2 surface. It is also clear that this island nonlinearly produces the (4,2) harmonic found in the magnetic data; in the ECE data, the 21.5 kHz harmonic peaks at the same location and has a phase flip at the same radii as the fundamental 10.75 kHz mode. In contrast, although the magnetic data suggest the presence of frequency-locked 3/1 and 3/2 modes, evidence for their existence is absent in the ECE data. Accordingly, in the subsequent analysis, we consider cases with and without accompanying 3/2 and 3/1 harmonics.

The vector potential of a magnetic island is represented by $\boldsymbol{A}_{||} = \alpha \boldsymbol{B}_0$ in the GTC. Here, $\alpha = \alpha_{mn}\cos(m\theta - n\zeta)$ represents the amplitude and helicity of the magnetic island. It produces a magnetic island at the rational surface with a width[27] of $\delta\psi_0 = 4\sqrt{\alpha_{mn}/s}$, where $s = q'/q$ is the local shear and primes denote derivatives with respect to the poloidal flux ψ. Therefore, we need to get the island amplitude α_{mn} from $\delta\psi$ in Fig. 3(b). By definition, $\delta\psi_0$ corresponds to the perturbation value at the island separatrices and $\delta\psi = 0$ at the island center. Since NTM can flatten the electron temperature, the width of the flattened region can be used to estimate the width of the island. In Figs. 3(a) and 3(b), the separatrices of the 2/1 island are shown by the two vertical black lines. We determine the black lines by using the width of the T_e flattened region and by assuming that the island is symmetrical about the resonant surface $q_s = 2$ (the purple line). The above method to identify the island separatrices is somewhat subjective. In Fig. 3(b), $\delta\psi_{inner}$ and $\delta\psi_{outer}$ correspond to the perturbation values of the inner and outer separatrices of the magnetic island, respectively. We calculate $\delta\psi_0$ from $2\delta\psi_0 = |\delta\psi_{inner} - \delta\psi_{outer}|$. Then, we calculate the island amplitude α_{mn} by using $\delta\psi_0 = 4\sqrt{\alpha_{mn}/s}$. This method does not take into account the kink, interchange, and toroidicity effects on the island structure.

Since the magnetic 2/1 island is the dominant mode, it is relatively straightforward to determine the separatrices of the magnetic island. However, for the 3/2 island or the 3/1 island, the island width is so small that we can no longer determine the width of the magnetic island based on the width of the flattened region of the electron temperature. Therefore, we adopt another way to calculate the widths of the 3/1 and 3/2 islands. Since the width of the 3/2 island is too small, we consider the two nearest extremal points of $\partial T_e^2/\partial^2\psi$ on the left and right sides of the resonant surface $q_s = 3/2$ as the inner ($\delta\psi_{\text{inner}}$) and outer ($\delta\psi_{\text{outer}}$) separatrices. We can use the same method to get the amplitude of the 3/1 island. The 3/2 island separatrices and 3/1 island separatrices are labeled by purple and green dotted lines in Fig. 3(b), respectively. The island width depends sensitively on the magnetic shear and the amplitude of the helical function α on the rational surface. It is not very sensitive to the exact functional form of the α function. So, we adopt a Gaussian function for α_{mn}, which peaks at the resonant surface. The width of the Gaussian function we used is approximately equal to the width of the magnetic island. The radial profiles of the scalar function α_{mn} and safety factor q are shown in Fig. 3(c), indicating the amplitude of $\alpha_{21} = 1.9 \times 10^{-4}$, for the 2/1 island, $\alpha_{32} = 2.97 \times 10^{-6}$ for the 3/2 island, and $\alpha_{31} = 9.87 \times 10^{-6}$ for the 3/1 island. To include multiple islands in a GTC simulation, multiple m and n harmonics can be added up, i.e., $\alpha = \sum_{m,n} \alpha_{mn}\cos(m\theta - n\zeta)$.

The poloidal structure of the 2/1 island expressed by helical flux function $\psi_{he} = \psi - \frac{\psi_s}{q_s} - \alpha g$ is shown in Fig. 4, which satisfies the condition $(\boldsymbol{B}_0 + \delta\boldsymbol{B}_I) \cdot \nabla\psi_{he} = 0$. The width of the 2/1 island is about 10 cm, and the minor radius is about 49.7 cm. We assume that the island rotation is caused by a radial electric field, which also causes the EP guiding center E × B drift. So, we transform to the rotating frame, where the island is static. The phases of islands in our simulation are then set to be zero. The width of the 3/2 island is about 0.8 cm, and the width of the 3/1 island is about 1.5 cm. The island width inferred from the ECE data has been compared with that from magnetics for a similar shot in Ref. 3, and the two measurements are consistent within experimental uncertainties. Note that, by changing the amplitude of α_{mn}, we can scan the effects of different island widths on the EP distribution function.

IV. RE-DISTRIBUTION OF EPS BY STATIC MAGNETIC ISLANDS

We first focus on the re-distribution of EPs by the 2/1 magnetic island along the radial direction. GTC simulations find that the radial profile of EPs is partially flattened within the island regions. The change of the density $(N_2 - N_1)/N_0$ in the (ψ, θ) plane in the low field side ($\theta = 0$) can be clearly seen in Fig. 5, where N_2 is the distribution modified by the 2/1 island, N_1 is the distribution without an island, and N_0 is the average number of particles on the grid. This density in the poloidal cross section is averaged over a small range of the toroidal angle $\zeta = 0 \pm 0.02$, and the black dots are the structure of the 2/1 island. Furthermore, the coupling between the island perturbation

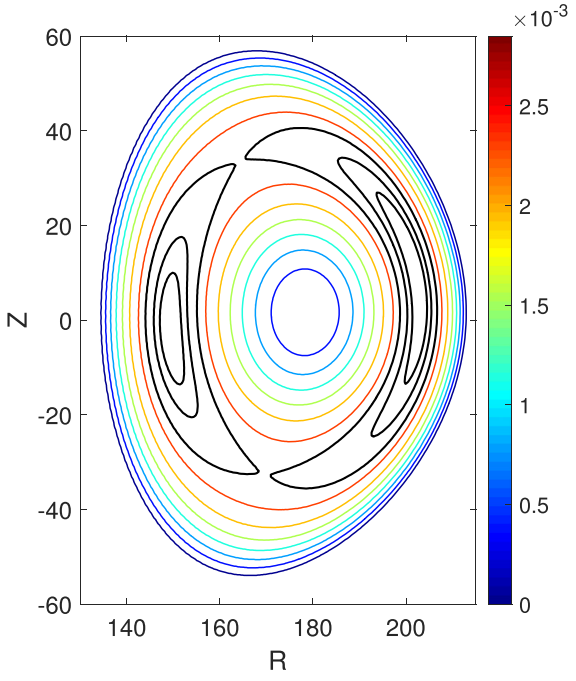

FIG. 4. Poloidal structure of the 2/1 island. The color of lines indicates the value of helical flux ψ_{he}. The black lines highlight the island structure inside the separatrices.

Published under license by AIP Publishing

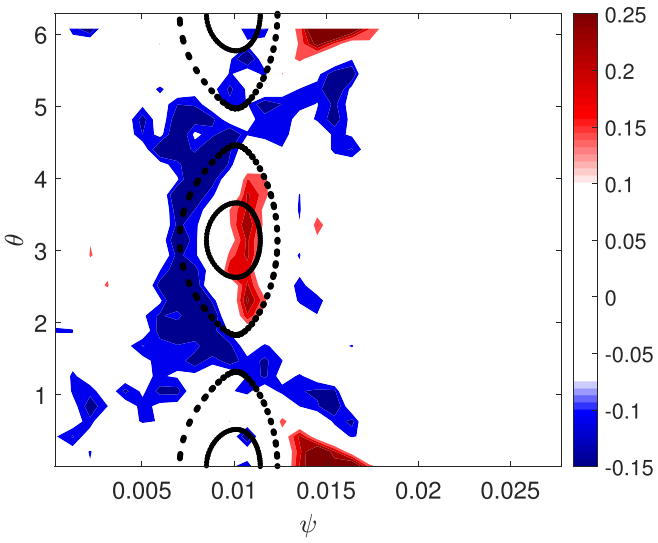

FIG. 5. The poloidal cross section profile of the EP density difference $(N_2 - N_1)/N_0$ at $\zeta = 0 \pm 0.02$ between the case with the 2/1 island and the case without an island.

and the background magnetic field produces higher-order islands in the particle phase space. Therefore, there are multiple islands in the particle phase space. It is possible for the two adjacent phase space islands to overlap when they are large enough, and the corresponding particle trajectories become stochastic. The stochasticity threshold is given by the condition that the widths of two adjacent phase space islands exceed the Chirikov criterion $w_2 + w_1 > r_2 - r_1$, where w_2 and w_1 are the half widths of the two adjacent phase space islands and r_2 and r_1 are the radial locations of the two adjacent phase space islands, respectively.

We assess the effects of the magnetic island on the EP distribution function by making a Poincare plot for the particle drift surface, which we refer to as a kinetic Poincare plot to differentiate it from the Poincare plot of the magnetic field lines. We select an EP with an energy $E = 40$ keV and a pitch angle $\lambda = \frac{v_\parallel}{v} = 1$. The points of particle trajectories are plotted in the poloidal cross section (ψ, θ) at $\zeta = 0$ in Fig. 6, where the color of lines represents the value of ψ. Although we only load the magnetic island perturbation α_{21}, there exist $m = 2$ and $m = 3$ harmonics in the particle phase space, and they can couple with each other to create other harmonics and even stochastic regions. Particles with high energy and a low pitch angle are more likely to become stochastic because the curvature drifts and grad-B drifts are much larger.[33] In this 2/1 island, $E = 15$ keV is the stochasticity threshold for an EP with $\lambda = 1$, which is useful to predict the stochasticity of EPs in the experiment. Since particles with different energies and pitch angles have different stochastic regions in the phase space, we can use different island perturbations for ash removal and impurity control.[33] These island perturbations should be small to avoid significant effects on the global confinement but large enough to select some kinds of particles to remove from the tokamak.

We then add the three magnetic islands of 3/2, 2/1, and 3/1 in Fig. 3(c) to study the effects of multiple islands on EPs. Figure 7 shows the magnetic field lines in the case with multiple islands, where the color of lines represents the value of ψ. If the island widths are large enough to satisfy the Chirikov criterion, the linear superposition of the multiple helical functions (i.e., co-existence of multiple islands) can generate other islands in magnetic field lines, even stochastic regions in real space. However, our simulations find that the stochasticity of magnetic field lines has little impact on the EP re-distribution. The flattening effects of the 2/1 island is still dominant, i.e., $(N_2 - N_1)/N_0$

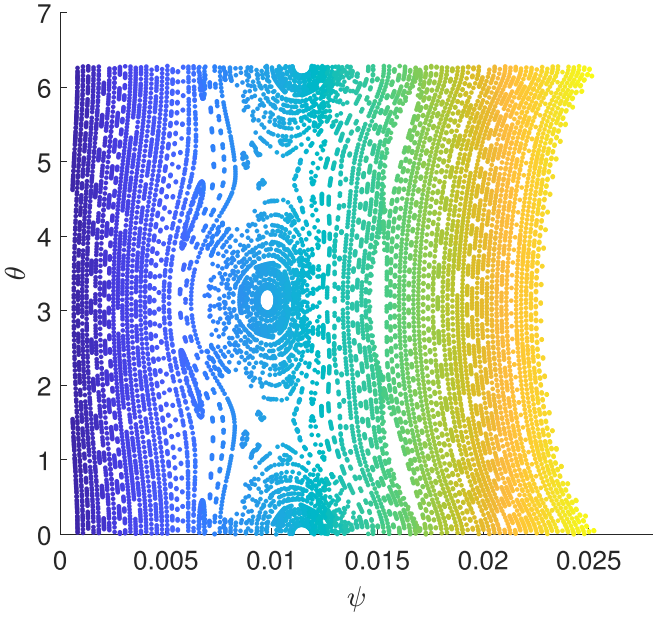

FIG. 6. Kinetic Poincare plot at the $\zeta = 0$ poloidal cross section for EPs with $E = 40$ keV and $\lambda = 1$ in the presence of the 2/1 island.

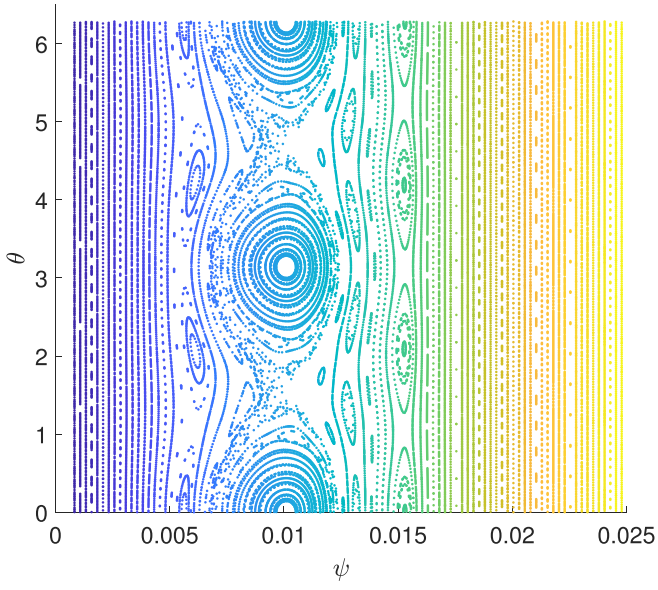

FIG. 7. The Poincare plot of magnetic field lines in the poloidal (ψ, θ) plane at $\zeta = 0$ with 3/2, 2/1, and 3/1 islands.

Published under license by AIP Publishing

is almost the same between the case with 3 islands and the case with the 2/1 island alone.

Next, we investigate the EP re-distribution in the phase space using constants of motion. Since the islands in our simulation are not time dependent, the particle energy and magnetic moment are conserved, while the canonical momentum P_ζ is not conserved due to the breaking of toroidal symmetry. The definition of canonical momentum is given by

$$P_\zeta = g\rho_{||} - \psi,$$

where $\rho_{||} = v_{||}/\Omega_p$ is the effective parallel gyroradius. The contour plot of $(N_2 - N_1)/N_0$ in the $(P_\zeta/\psi_X, E)$ plane at $\zeta = 0 \pm 0.02$ is shown in Fig. 8(a), where N_2 is the distribution with the 2/1 island, ψ_X is the poloidal flux of the last closed magnetic field lines, and E is normalized to $m_p R_0^2 \Omega_p^2$. In Fig. 8(a), we can see the differences of the density in the $(P_\zeta/\psi_X, E)$ plane peak at $\frac{P_\zeta}{\psi_X} \sim -0.3$ and the EP moving outward to flatten the density profile. Since the first term $g\rho_{||}$ is smaller than the second term ψ in the definition of P_ζ, the change in the distribution mainly occurs around the $q_s = 2/1$ resonant surface, where $P_\zeta/\psi_X \approx -\psi_{2/1}/\psi_X = -0.34$. The results demonstrate the flattening effect of the magnetic island in the phase space of constants of motion. We plot the domains of confined particles for a fixed value of μ in Fig. 8(b), which shows the change in the distribution function between the case with the 2/1 island and the case without the island for $\mu B_0 = 60 \pm 2$ keV. The red line is the loss boundary for co-moving particles with orbits touching the outer midplane, the blue line represents the orbits that pass through the magnetic axis, and the green line is the loss boundary for counter-moving particles with orbits touching the inner midplane. This plot shows the confined co-passing ($P_+ - C$), confined trapped (T-C), trapped loss (T-L), confined counter-passing ($P_- - C$), and counter-passing loss ($P_- - L$) domains. We can see that the change in the distribution function mainly occurs in the domain of confined trapped particles. The domain of confined co-passing also has some differences, but they are smaller than that of confined trapped particles.

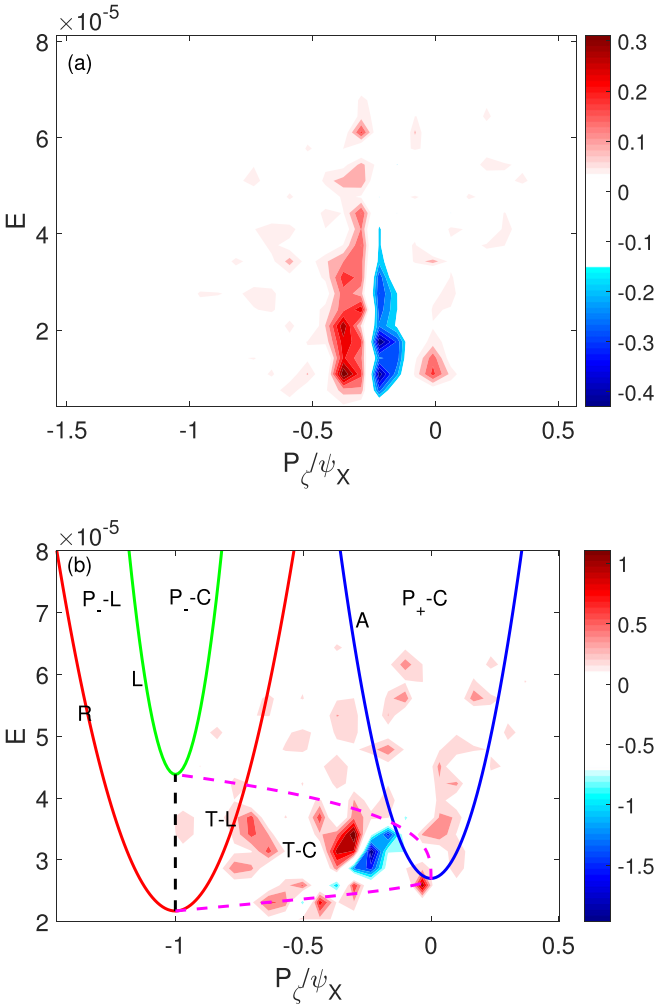

FIG. 8. (a) The contour plot of $(N_2 - N_1)/N_0$ at $\zeta = 0 \pm 0.02$ after integrating over all particles. (b) The confined particle plane in $(P_\zeta/\psi_X, E)$ for EPs with $\mu B_0 = 60 \pm 2$ keV. The apexes of the parabolas are at $E = \mu B_{max}$(green line), $E = \mu B_0$(blue line), and $E = \mu B_{min}$(red line), and the dashed line is the trapped-passing boundary.

In the process of the EP re-distribution, the 2/1 island can induce outward radial particle flux around resonant surface $q_s = 2/1$. In our simulation, the particle flux gradually decreases to zero when the EP distribution establishes a new steady-state after about $20(R_0/C_s)$, where $C_s = \sqrt{T_e/m_i}$. The definition of particle flux is $\Gamma = \int (v_{||}\frac{\delta B_r}{B_0} + v_{dr}) f dv$, where v_{dr} is the radial component of the magnetic drift velocity. Flux-surface averaging is applied to all fluxes when calculating the particle flux.

Since the initial EP distribution function used in our simulation is a local Maxwellian, it is not a neoclassical solution that satisfies the drift kinetic equation in the toroidal geometry. The EP distribution function evolves to reach a neoclassical steady-state solution after a few transit times (in the collisionless limit). In the simulation, the effect of island perturbation on particle motion is first turned off. After a short time, when the EP distribution function achieves a neoclassical steady-state, the island perturbation is turned on, which induces a particle flux. In Fig. 9(a), the red line represents the particle flux corresponding to the case with the 2/1 island only, the purple line represents that corresponding to the case with multiple islands 2/1, 3/2, and 3/1, and the blue line represents that corresponding to the case with the multiple islands as the purple line but with a larger 3/2 island (which is increased to 1.2 cm). We can see that the EP distribution function gradually achieves a new steady-state, and the particle fluxes decrease to almost zero after some time.

If we integrate particle fluxes over time before 12 R_0/C_s, we can get the radial profiles of the particle fluxes as shown in Fig. 9(b). The particle fluxes are relatively positive around the resonant surface $q_s = 2/1$, which means that EPs move outward across the islands. In Fig. 9(b), particle fluxes are almost the same for the case with multiple islands (purple line) and the case with a single island (red line). This is probably because the drift orbit widths of most EPs are larger than the width of the stochastic regions, which is about 1.5 cm. For a particle with $E = 40$ keV and $\lambda = 0.4$, the half width of the banana orbit around the $q_s = 2$ resonant surface is about 7.6 cm. However, for the other case with an increased width of the 3/2 island, the region

Published under license by AIP Publishing

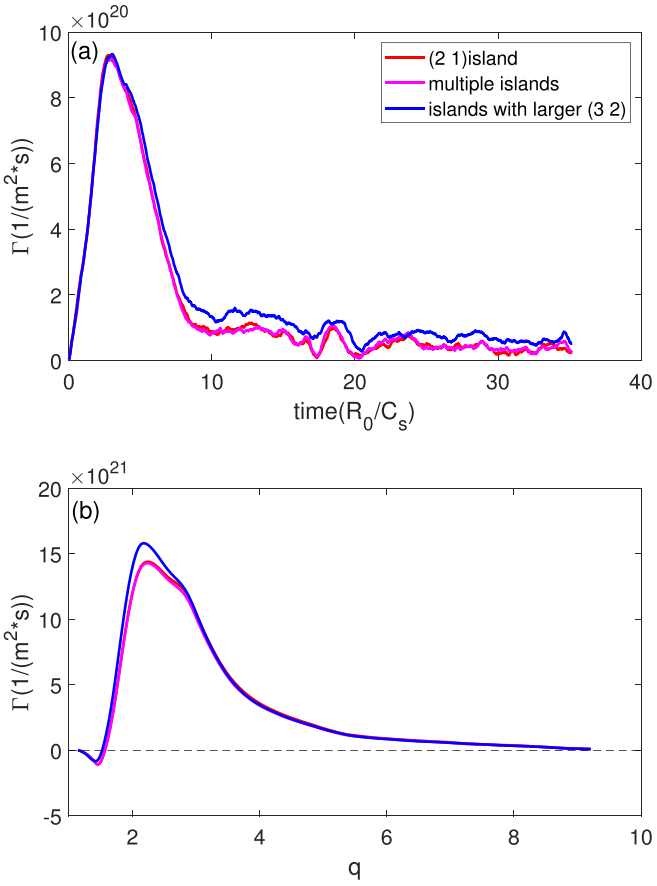

FIG. 9. (a) Time history of particle fluxes induced by magnetic islands in the simulations. (b) Particle fluxes as a function of the radial coordinate represented by safety factor q after integrating over time before 12 R_0/C_s.

between the 2/1 island and the 3/2 island is mostly stochastic. Since the width of this stochastic region is about 12 cm, which is much larger than the EP drift orbit width, the particle flux (blue line) is larger than the one with only the 2/1 island, as shown in Fig. 9(b). Therefore, only when the width of stochastic regions is larger than the EP drift orbit width, it can cause significant particle flux. Our work focuses on the transport across the magnetic islands. The reason that particles do not leave the simulation domain is that the simulation domain is much wider than the island width to minimize the effects of the simulation boundary. The other transport mechanism outside the island region is needed for particles to be lost from the simulation domain.

Finally, we calculate the heat flux in our simulations. Similar to the particle flux, there is no heat flux in the absence of the magnetic island, which means that the heat flux is only induced by the magnetic island. The maximum of the surface-averaged heat flux is about $Q = 5.2\,\mathrm{MW/m^2}$ at $t = 5R_0/C_s$. In this shot (DIII-D #157402), there are no direct measurements of the EP heat flux in the plasma interior, but there are measurements of the heat flux to the wall. An infrared camera that views the tiles that surround mock-up test-blanket module coils registers an increase in the heat flux of 2–7 $\mathrm{MW/m^2}$ during the NTM activity.[34] Note that the heat flux calculated in GTC simulation is transient since the simulation has no EP sources to maintain EP pressure profiles. Moreover, the infrared camera measurement is not a flux surface-averaged quantity.[35] The island-induced prompt losses strongly depend on neutral beam injection locations. Therefore, in the experiment, toroidally and poloidally varying EP heat fluxes are expected, which is not captured by the camera. Thus, the comparison between simulations and experimental measurements of the EP heat flux is at best qualitative.

V. EP EFFECTS ON NTM

In this section, we study the EP effects on NTM excitation in the realistic equilibrium of DIII-D shot #170239 by a reduced resistive MHD model in the GTC.[21] In this linear NTM simulation model, thermal ions and electrons are treated using fluid models. We begin with the continuity equation for ion and electron species[36]

$$\begin{aligned} Z_\alpha \frac{\partial \delta n_\alpha}{\partial t} &+ \boldsymbol{B}_0 \cdot \nabla\left(\frac{Z_\alpha n_{0\alpha}\delta u_{||\alpha}}{B_0}\right) + \boldsymbol{\delta B}\cdot\nabla\left(\frac{Z_\alpha n_{0\alpha} u_{||0\alpha}}{B_0}\right) \\ &+ \boldsymbol{\delta B}\cdot\nabla\left(\frac{Z_\alpha n_{0\alpha}\delta u_{||\alpha}}{B_0}\right) + B_0 \boldsymbol{v_E}\cdot\nabla\left(\frac{Z_\alpha n_{0\alpha}}{B_0}\right) \\ &+ c\nabla\times\boldsymbol{b}_0\cdot\nabla\left(\frac{\delta p_{||\alpha}}{B_0}\right) + c\boldsymbol{b}_0\times\nabla B_0\cdot\nabla\left(\frac{\delta p_{\perp\alpha}}{B_0^2}\right) \\ &+ \frac{c\nabla\times\boldsymbol{b}_0\cdot\nabla B_0}{B_0^2}\delta p_{\perp\alpha} + \frac{c\nabla\times\boldsymbol{b}_0}{B_0}\cdot Z_\alpha n_{0\alpha}\nabla\delta\phi = 0. \end{aligned} \tag{5}$$

Here, index $\alpha = e$, and i stands for the particle species (electron or ion). If we define guiding center charge density $\delta\rho = \sum_\alpha q_\alpha \delta n_\alpha$ and parallel current $\delta j_{||} = \sum_\alpha q_\alpha n_{0\alpha}\delta u_{||\alpha}$, by subtracting the continuity equation of the electron from the continuity equation of the ion, we can get

$$\begin{aligned} &\frac{\partial\delta\rho}{\partial t} + \boldsymbol{B}_0\cdot\nabla\frac{\delta j_{||}}{B_0} + \boldsymbol{\delta B}\cdot\nabla\frac{j_{||0}}{B_0} + \boldsymbol{\delta B}\cdot\nabla\frac{\delta j_{||}}{B_0} \\ &+ c\nabla\times\boldsymbol{b}_0\cdot\nabla\frac{\delta p}{B_0} + c\boldsymbol{b}_0\times\nabla B_0\cdot\nabla\frac{\delta p}{{B_0}^2} + \frac{c\nabla\times b_0\cdot\nabla B_0}{{B_0}^2}\delta p = 0. \end{aligned} \tag{6}$$

We assume that the ion is cold and the fluid pressure is isotropic $\delta p = \delta p_{\perp e} = \delta p_{||e}$. The pressure diffusion equation is solved to recover the pressure flattening effect inside the island

$$\frac{d\delta p}{dt} = \chi_{||}\nabla_{||}^2\delta p + \chi_{||}\nabla_{||}\left(\frac{\delta\boldsymbol{B}}{B_0}\cdot\nabla p_0\right) + \chi_\perp\nabla_\perp^2\delta p, \tag{7}$$

where $\nabla_{||}$ and $\nabla_\perp$ are the gradient operators defined using the equilibrium magnetic field. In high temperature plasmas, the parallel heat conductivity $\chi_{||}$ is much larger than the perpendicular heat conductivity $\chi_\perp$. In our simulation, we use the perpendicular thermal diffusivity $\chi_\perp = 1\,\mathrm{m^2/s}$, the parallel thermal diffusivity $\chi_{||} = 1.0\times10^8\,\mathrm{m^2/s}$, and the resistivity $\eta = 9.0\times10^{-6}\,\Omega/\mathrm{m}$.

We use the electron momentum equation to evolve the parallel vector potential as

$$\frac{\partial\delta A_{||}}{\partial t} = -c\boldsymbol{b}_0\cdot\nabla\delta\phi + \frac{c}{n_{e0}e}\boldsymbol{b}_0\cdot\nabla\delta p + \frac{c}{n_{e0}e}\frac{\delta\boldsymbol{B}}{B_0}\cdot\nabla p_0 - \frac{\nu_{ei}m_e c}{e^2 n_{0e}}\delta j_e. \tag{8}$$

Published under license by AIP Publishing

The total perturbed current is $\delta j_{||} = \delta j_e + \delta j_{ep} + \delta j_{bs}$, and Ampére law is

$$\delta j_{||} = -\frac{c}{4\pi}\nabla_\perp^2 \delta A_{||}. \quad (9)$$

The bootstrap current model is written as[37]

$$\delta j_{bs} = -1.46\frac{\sqrt{\epsilon}}{B_\theta}\frac{\partial \delta p}{\partial r}, \quad (10)$$

where $\epsilon = r/R$.

The quasi-neutral condition can be written as

$$\frac{\omega_{pi}^2}{\Omega_i^2}\nabla_\perp^2 \phi = 4\pi\delta\rho. \quad (11)$$

Equations (6)–(11) form a closed reduced MHD system for thermal plasmas in the NTM simulation. The perturbed EP current is calculated using the gyrokinetic equation as described in Sec. II.

The DIII-D shot #170239 is designed to study the EP effects on NTM. Without bootstrap current, the tearing mode is stable, while the NTM (driven by bootstrap current) is unstable in this equilibrium. GTC simulation finds that the linear NTM growth rate without EPs is 0.026 R_0/C_s when we use a seed island width of 5.2 cm. Then, we add the perturbed current of EPs to study the EP effects on NTM instability.

We use the experimental data of the EP distribution function from TRANSP to calculate the perturbed current induced by a static island. The black dotted lines in Fig. 10(b) are the separatrices of the static 2/1 island with a width of 5.2 cm, which is used as the seed island in the GTC simulation. The EP density profile is plotted in Fig. 10(a), which peaks on axis, $n_{f0} = 1.4 \times 10^{13}\,\mathrm{cm}^{-3}$. Due to the flattening effect by the magnetic island on the EP distribution function, we can get a perturbed parallel EP current,

$$\delta j_{ep} = j_{ep} - j_{ep0} = \int \frac{v_{||} f}{(1+\varepsilon\cos\theta)}\mathrm{d}\mathbf{v} - \int \frac{v_{||} f_0}{(1+\varepsilon\cos\theta)}\mathrm{d}\mathbf{v}, \quad (12)$$

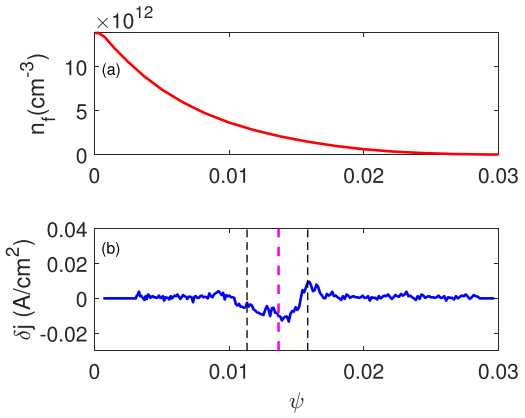

FIG. 10. The radial profile of (a) EP density and (b) perturbed EP current induced by the magnetic island.

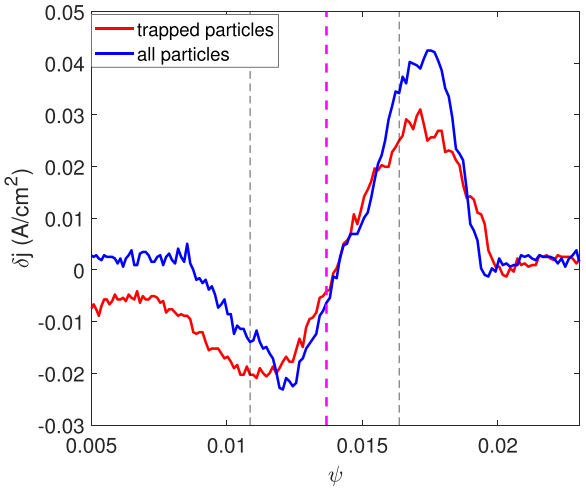

FIG. 11. The radial profile of perturbed EP current induced by the magnetic island.

where f is the distribution function of EPs in the presence of the magnetic island and f_0 is the distribution function without the magnetic island. This perturbed current is the un-shielded EP current.[38] In this shot, electron shielding[39] reduces the current to approximately 77% of the unshielded value. δj_{ep} is negative (the same direction as equilibrium bootstrap current) around the $q_s = 2/1$ surface, as shown in Fig. 10(b). This perturbed current mainly depends on the EP density and the width of the magnetic island. Our simulation shows that the linear growth rate of NTM is about 0.023 R_0/C_s in the presence of the perturbed EP current, a reduction of 12% when compared to that without EPs. Therefore, the perturbed EP current has a small stabilizing effect on the excitation of the 2/1 NTM, consistent with the observation[3] that the island width is decreased about 1 cm by fast ions in this DIII-D experiment.

Finally, we use a large magnetic island ($w_d = 10$ cm) to calculate the perturbed currents, and the simulation results are shown in Fig. 11. The purple line is the location of the $q_s = 2/1$ surface, and the black dotted lines are the island separatrices. We can see that the perturbed current is mainly contributed by trapped EPs. These results show that trapped EPs can have a stronger interaction with the magnetic islands. There are typically less trapped fast ions from tangential NBI but more trapped fast ions from ion cyclotron resonant heating (ICRH) and more trapped α-particles in burning plasmas.

VI. SUMMARY

In this work, we have carried out global gyrokinetic toroidal code (GTC) simulations using realistic DIII-D equilibrium to study the interactions between energetic particles (EPs) and neoclassical tearing mode (NTM) islands. NTM islands can partially flatten the radial profile of the EP density in the island regions. In the EP phase space using constants of motions $(P_\zeta/\psi_X, E)$, the change in the EP distribution function mainly occurs in the domain of confined trapped particles, consistent with the experimental observation[8] that the trapped EPs strongly interact with the NTM. Using a single magnetic island, GTC simulations find that stochastic regions exist in the EP phase space

Published under license by AIP Publishing

when nonlinear harmonics overlap with each other.[11,33] The EP radial particle flux is induced around the dominant magnetic island region and decreases over time to almost zero in the absence of EP sources. The particle flux induced by three magnetic islands (3/2, 2/1, and 3/1) is almost the same as that by a single dominant 2/1 island when the width of stochastic regions is small compared to the EP orbit width. If we increase the width of the 3/2 island from 0.8 cm to 1.2 cm, the entire regions between the 2/1 island and the 3/2 island become stochastic, which leads to a significant increase in the particle flux. Finally, we study the EP effects on the NTM instability in a realistic DIII-D equilibrium by using a reduced resistive MHD model in GTC simulations. We find that the perturbed parallel EP current induced by the magnetic islands can reduce the NTM growth rate, but the effect is modest. Our simulations demonstrate the re-distribution of EPs by low-n static magnetic islands.[8,11] While the passing EPs contribute to the flattening of the radial density profile, the trapped particles interact with the magnetic island strongly and can contribute more to the perturbed EP current.

In the current simulation, the frequency of the magnetic islands is assumed to be zero. However, the magnetic island frequency can be finite, which can affect the EP re-distribution,[12] especially when multiple islands rotate with different frequencies. In the future, we will include the finite island frequency in our simulations. Moreover, our NTM simulations find that EP current induced by the magnetic islands has a weak stabilization effect. The effect of this current is smaller than that of the uncompensated cross field current due to the charge separation when the EP orbit width is much larger than the island width.[17] Therefore, our future study should contain the kinetic effects of EPs self-consistently in the NTM simulations in order to study the EP effects on the NTM comprehensively. We will also perform self-consistent simulations including nonlinear coupling of the magnetic islands.

ACKNOWLEDGMENTS

The authors would like to acknowledge the useful discussions with the GTC Team. This work was supported by the China National Magnetic Confinement Fusion Science Program (Grant No. 2018YFE0304100), the U.S. Department of Energy, Office of Science, Office of Advanced Scientific Computing Research and Office of Fusion Energy Sciences, and the Scientific Discovery through Advanced Computing (SciDAC) program under Award No. DE-SC0018270 (SciDAC ISEP Center). This material is based upon the work supported in part by the U.S. Department of Energy, Office of Science, Office of Fusion Energy Sciences, using the DIII-D National Fusion Facility, a DOE Office of Science user facility, under Award No. DE-FC02-04ER54698. This work used resources of the Oak Ridge Leadership Computing Facility at the Oak Ridge National Laboratory (DOE Contract No. DE-AC05-00OR22725) and the National Energy Research Scientific Computing Center (DOE Contract No. DE-AC02-05CH11231).

This report was prepared as an account of the work sponsored by an agency of the United States Government. Neither the United States Government nor any agency thereof, nor any of their employees, makes any warranty, express or implied, or assumes any legal liability or responsibility for the accuracy, completeness, or usefulness of any information, apparatus, product, or process disclosed, or represents that its use would not infringe privately owned rights. Reference herein to any specific commercial product, process, or service by trade name, trademark, manufacturer, or otherwise does not necessarily constitute or imply its endorsement, recommendation, or favoring by the United States Government or any agency thereof. The views and opinions of the authors expressed herein do not necessarily state or reflect those of the United States Government or any agency thereof.

REFERENCES

[1]P. C. de Vries, M. F. Johnson, B. Alper, P. Buratti, T. C. Hender, H. R. Koslowski, V. Riccardo, and JET-EFDA Contributors, Nucl. Fusion **51**(5), 053018 (2011).
[2]R. B. White and H. E. Mynick, Phys. Fluids B **1**, 980 (1989).
[3]W. W. Heidbrink, L. Bardoczi, C. S. Collins, G. J. Kramer, R. J. La Haye, D. J. Lin, C. M. Muscatello, M. Podestà, L. Stagner, and M. A. Van Zeeland, Nucl. Fusion **58**, 082027 (2018).
[4]E. M. Carolipio, W. W. Heidbrink, C. B. Forest, and R. B. White, Nucl. Fusion **42**, 853–862 (2002).
[5]S. J. Zweben, D. S. Darrow, E. D. Fredrickson, G. Taylor, S. von Goeler, and R. B. White, Nucl. Fusion **39**, 1097 (1999).
[6]M. Garcia-Munoz, P. Martin, H.-U. Fahrbach, M. Gobbin, S. Günter, M. Maraschek, L. Marrelli, H. Zohm, and the ASDEX Upgrade Team, Nucl. Fusion **47**, L10 (2007).
[7]M. Gobbin, L. Marrelli, H. U. Fahrbach, M. Garcia-Muñoz, S. Günter, P. Martin, R. B. White, and the ASDEX Upgrade Team, Nucl. Fusion **49**, 095021 (2009).
[8]L. Bardoczi, M. Podesta, W. W. Heidbrink, and M. A. Van Zeeland, Plasma Phys. Controlled Fusion **61**, 055012 (2019).
[9]S. J. Zweben, R. L. Boivin, R. E. Duvall, E. D. Fredrickson, R. J. Goldston, H. E. Mynick, J. D. Strachan, and R. B. White, Phys. Fluids B **2**(6), 1411–1414 (1990).
[10]C. B. Forest, J. R. Ferron, T. Gianakon, R. W. Harvey, W. W. Heidbrink, A. W. Hyatt, R. J. La Haye, M. Murakami, P. A. Politzer, and H. E. St. John, Phys. Rev. Lett. **79**, 427 (1997).
[11]H. E. Mynick, Phys. Fluids B **5**, 2460 (1993).
[12]R. B. White, Commun. Nonlinear Sci. Numer. Simul. **17**, 2200 (2012).
[13]S. Sesnic, S. Günter, A. Gude, M. Maraschek, and ASDEX Upgrade Team, Phys. Plasmas **7**, 935 (2000).
[14]E. Li, V. lgochine, L. Xu, T. Shi, H. Zhao, Y. Liu, A. Ti, R. White, J. Zhang, Y. Zhu, J. Huang, B. Shen, S. Lin, J. Qian, X. Gong, L. Hu, and EAST Contributors, Plasma Phys. Controlled Fusion **58**, 045012 (2016).
[15]H. Cai, S. Wang, Y. Xu, J. Cao, and D. Li, Phys. Rev. Lett. **106**, 075002 (2011).
[16]H. Cai and G. Fu, Phys. Plasma **19**, 072506 (2012).
[17]H. Cai, Nucl. Fusion **56**, 126016 (2016).
[18]R. J. Buttery, R. J. La Haye, P. Gohil, G. L. Jackson, H. Reimerdes, E. J. Strait, and the DIII-D Team, Phys. Plasmas **15**, 056115 (2008).
[19]C. C. Hegna and A. Bhattacharjee, Phys. Rev. Lett. **63**, 2056 (1989).
[20]T. C. Hender, J. C. Wesley, J. Bialek, A. Bondeson, A. H. Boozer, R. J. Buttery, A. Garofalo, T. P. Goodman, R. S. Granetz, and Y. Gribov, Nucl. Fusion **47**, S128 (2007).
[21]K. Wang, C. Xiao, W. Zhang, and Z. Lin, "Verification of gyrokinetic particle simulation of current-driven instability in fusion plasmas. V. Neoclassical tearing modes" (unpublished).
[22]Z. Lin, T. S. Hahm, W. W. Lee, W. M. Tang, and R. B. White, Science **281**, 1835 (1998).
[23]P. Jiang, Z. Lin, I. Holod, and C. Xiao, Phys. Plasma **21**, 122513 (2014).
[24]K. S. Fang and Z. Lin, Phys. Plasmas **26**, 052510 (2019).
[25]G. Dong and Z. Lin, Nucl. Fusion **57**, 036009 (2017).
[26]W. W. Lee, J. Comput. Phys. **72**, 243 (1987).

Published under license by AIP Publishing

[27]R. B. White, *The Theory of Toroidally Confined Plasmas*, 3rd ed. (Imperial College Press, 2014).
[28]A. Brizard and T. S. Hahm, Rev. Mod. Phys. **79**, 421 (2007).
[29]I. Holod, W. L. Zhang, Y. Xiao, and Z. Lin, Phys. Plasma **16**, 122307 (2009).
[30]R. V. Budny, Nucl. Fusion **34**, 1247 (1994).
[31]M. E. Austin and J. Lohr, Rev. Sci. Instrum. **74**, 1457 (2003).
[32]L. Bardoczi, T. L. Rhodes, T. A. Carter, N. A. Crocker, W. A. Peebles, and B. A. Grierson, Phys. Plasma **23**, 052507 (2016).
[33]H. E. Mynick, Phys. Fluids B **5**, 1471 (1993).
[34]W. W. Heidbrink, M. E. Austin, C. S. Collins, T. Gray, B. A. Grierson, G. J. Kramer, M. Lanctot, D. C. Pace, M. A. Van Zeeland, and A. G. Mclean, Nucl. Fusion **55**, 083023 (2015).
[35]G. J. Kramer, A. McLean, N. Brooks, R. V. Budny, X. Chen, W. W. Heidbrink, T. Kurki-Suonio, R. Nazikian, T. Koskela, and M. J. Schaffer, Nucl. Fusion **53**, 123018 (2013).
[36]W. Deng, Z. Lin, and I. Holod, Nucl. Fusion **52**, 023005 (2012).
[37]F. L. Hinton and R. D. Hazeltine, Rev. Mod. Phys. **48**, 239 (1976).
[38]M. Honda, M. Kikuchi, and M. Azumi, Nucl. Fusion **52**, 023021 (2012).
[39]P. A. Politzer and G. D. Porter, Nucl. Fusion **30**, 1605 (1990).

Published under license by AIP Publishing